







Probing Multiple Populations of Compact Binaries with Third-generation Gravitational-wave Detectors

Ken K. Y. Ng^{1,2} , Salvatore Vitale^{1,2} , Will M. Farr^{3,4} , and Carl L. Rodriguez⁵ 

¹ LIGO Laboratory, Massachusetts Institute of Technology, Cambridge, MA 02139, USA; kenkyng@mit.edu

² Kavli Institute for Astrophysics and Space Research, Massachusetts Institute of Technology, Cambridge, MA 02139, USA

³ Department of Physics and Astronomy, Stony Brook University, Stony Brook, NY 11794, USA

⁴ Center for Computational Astrophysics, Flatiron Institute, 162 Fifth Avenue, New York, NY 10010, USA

⁵ McWilliams Center for Cosmology, Department of Physics, Carnegie Mellon University, 5000 Forbes Ave., Pittsburgh, PA 15213, USA

Received 2021 January 30; revised 2021 April 9; accepted 2021 April 15; published 2021 May 18

Abstract

Third-generation (3G) gravitational-wave detectors will be able to observe binary black hole mergers (BBHs) up to a redshift of ~ 30 . This gives unprecedented access to the formation and evolution of BBHs throughout cosmic history. In this paper, we consider three subpopulations of BBHs originating from the different evolutionary channels: isolated formation in galactic fields, dynamical formation in globular clusters, and mergers of black holes formed from Population III (Pop III) stars at very high redshift. Using input from population synthesis analyses, we create 2 months of simulated data of a network of 3G detectors made of two Cosmic Explorers and one Einstein Telescope consisting of $\sim 16,000$ field and cluster BBHs, as well as ~ 400 Pop III BBHs. First, we show how one can use a nonparametric model to infer the existence and characteristics of a primary and secondary peak in the merger rate distribution as a function of redshift. In particular, the location and height of the secondary peak around $z \approx 12$, arising from the merger of Pop III remnants, can be constrained at the $\mathcal{O}(10\%)$ level (95% credible interval). Then we perform a modeled analysis using phenomenological templates for the merger rates of the three subpopulations and extract the branching ratios and characteristic parameters of the merger rate densities of the individual formation channels. With this modeled method, the uncertainty on the measurement of the fraction of Pop III BBHs can be improved to $\lesssim 10\%$, while the ratio between field and cluster BBHs can be measured with an uncertainty of $\sim 100\%$.

Unified Astronomy Thesaurus concepts: [Gravitational waves \(678\)](#); [Gravitational wave sources \(677\)](#); [Gravitational wave astronomy \(675\)](#)

1. Introduction

Advanced gravitational-wave (GW) detectors such as LIGO (Aasi et al. 2015), Virgo (Acernese et al. 2015), and Kagra (Aso et al. 2013) have dramatically increased our ability to study stellar mass black holes (BHs) and the environments in which they form. The latest catalog released by the LIGO-Virgo-Kagra (LVK) collaboration includes 39 new GW detections, most of which are binary BHs (BBHs), bringing the total number of stellar mass BHs detected with GWs to over 100 (Abbott et al. 2019a, 2020a). These observations have already allowed for interesting astrophysical measurements (Abbott et al. 2019a, 2019b, 2020a, 2020b), such as hints of multiple formation channels (Farr et al. 2017; Zevin et al. 2017; Antonini & Gieles 2020; Belczynski et al. 2020; Zevin et al. 2021; Callister et al. 2020a; Wong et al. 2021b), hierarchical mergers (Fishbach et al. 2017; Gerosa & Berti 2017; Doctor et al. 2019; Kimball et al. 2019, 2020b; Gerosa et al. 2020; Tiwari & Fairhurst 2020), and constraints on stellar physics (Farmer et al. 2020; Fragione & Loeb 2021; Bavera et al. 2021), primordial BHs (Bird et al. 2016; Sasaki et al. 2016; Ali-Haïmoud et al. 2017; Boehm et al. 2020; Hall et al. 2020; Hütsi et al. 2021; Wong et al. 2021a), and ultralight bosons (Arvanitaki et al. 2017; Brito et al. 2017; Ng et al. 2021a, 2021b). Therefore, the growing set of BBHs enables the study of the properties of both individual sources and the underlying populations.

Among the key questions that can be addressed by GW astrophysics are how many such populations exist and what their characteristics are. Multiple approaches have been proposed to address these questions, which ultimately rely on looking for features that would be expected in the BBH generated by each

channel, such as their mass and spin distribution (Stevenson et al. 2015; Vitale et al. 2017; Fishbach & Holz 2017; Farr et al. 2017, 2018; Talbot & Thrane 2017, 2018; Bouffanais et al. 2019; Doctor et al. 2019; Fishbach et al. 2020; Fishbach & Holz 2020; Miller et al. 2020; Safarzadeh et al. 2020; Kimball et al. 2020a), eccentricity distribution (Lower et al. 2018), or redshift distribution (Fishbach et al. 2018; Callister et al. 2020b). However, due to the limited sensitivity of current GW detectors, the observed BBHs are relatively “local,” with redshift $z \lesssim 1$ (Abbott et al. 2019a, 2019b, 2020a, 2020b; Roulet et al. 2020; Venumadhav et al. 2020). Even as LIGO, Virgo, and Kagra improve their sensitivities with the implementation of frequency-dependent quantum squeezing (McCuller et al. 2020) and better low-frequency isolation (Yu et al. 2018), the detector horizon will reach $z \sim 3$ only for the heaviest systems (Abbott et al. 2016; Hall & Evans 2019).

Second-generation detectors will therefore be unable to access mergers at redshifts larger than a few. This likely precludes the possibility of detecting binaries whose component BHs originated directly from the Population III (Pop III) stars, whose formation peak could be as high as $z \sim 10$. Primordial BHs (Kinugawa et al. 2014, 2016; Hartwig et al. 2016; Belczynski et al. 2017; Raidal et al. 2017, 2019) might also be out of reach for existing facilities.⁶ This will not be the case in the era of third-generation (3G) GW detectors such as the Cosmic Explorer (CE; Abbott et al. 2017;

⁶ We note that there are studies suggesting that the heaviest BBH detected in the first part of the LIGO/Virgo O3 run, GW190521 (Abbott et al. 2020c, 2020d), may be a Pop III BBH (Kinugawa et al. 2021; Tanikawa et al. 2020).

Reitze et al. 2019) and Einstein Telescope (ET; Punturo et al. 2010; Van Den Broeck 2012; Maggiore et al. 2020). In fact, 3G detectors will have horizons up to $z \gtrsim 30$ and enable access to most of the BBHs throughout the cosmic history (Hall & Evans 2019). Therefore, both detections and nondetections of high-redshift BBHs with 3G detectors can provide significant constraints on the properties of Pop III remnants. This is particularly important, as the remnants of Pop III stars might be the light seeds that lead to the formation of supermassive BHs early in cosmic history (Greene et al. 2020). Whereas the space-based GW detector LISA (Amaro-Seoane et al. 2017) and electromagnetic missions such as the X-ray observatory Lynx (Gaskin et al. 2019) might reveal the presence of heavy (i.e., $M \gtrsim 100 M_{\odot}$) BHs at redshifts of 10, ground-based 3G detectors might very well be the only way to search for smaller building blocks: stellar mass BHs.

Using the current local BBH merger rate estimate, $\sim 25 \text{ Gpc}^{-3} \text{ yr}^{-1}$ (Abbott et al. 2020b), the total merger rate of the BBHs in the universe is inferred to be $\sim 10,000 \text{ month}^{-1}$, if the merger rate density follows the same evolution as the star formation rate (SFR; Regimbau et al. 2017). Nearly all of these BBHs would be detectable by 3G detectors, most of which will also have a very high signal-to-noise ratio (S/N), leading to very precise distance (and hence redshift, assuming a known cosmology) measurements (Vitale 2016; Vitale & Evans 2017; Vitale & Whittle 2018). The large number of loud observations thus allows for inferring the morphology of merger rate densities in both parametric and nonparametric ways (Van Den Broeck 2014; Safarzadeh et al. 2019; Vitale et al. 2019; Romero-Shaw et al. 2020). In Vitale et al. (2019), we showed how, by combining redshift measurements of tens of thousands of GW observations in 3G detectors and assuming that all BBHs are formed in galactic fields, one can infer the SFR history and time-delay distribution. In light of the properties of the BBHs detected by LIGO and Virgo in the last few years, it has become harder to assume that all BHs are formed in galactic fields, since many of the BHs being detected are consistent with having formed dynamically, in globular or nuclear clusters, or in the disks of active galactic nuclei (AGN; Bartos et al. 2017; Yi & Cheng 2019; Yang et al. 2019, 2020; Gröbner et al. 2020; Samsing et al. 2020; Tagawa et al. 2020a, 2020b, 2021). In this paper, we greatly extend our previous work (Vitale et al. 2019) and explore the possibility of simultaneously identifying and constraining the properties of multiple formation channels. In particular, we simulate universes where BHs can be formed in galactic fields and globular clusters and from Pop III stars. We show how well one can constrain the properties of each channel and their branching ratios. In particular, we focus on the evidence for a high-redshift ($z \gtrsim 5$) population, which would be the smoking gun of formation outside of the traditional evolutionary pathways.

2. Astrophysical Models

In this section, we summarize the main astrophysical properties of the BBH formation channels that we consider in the paper. Astrophysical BBHs are believed to form in various environments, such as binary stellar evolution in galactic fields (Dominik et al. 2012, 2013, 2015; de Mink & Belczynski 2015; Belczynski et al. 2016; O’Shaughnessy et al. 2017; Stevenson et al. 2017; Broekgaarden et al. 2019; Mapelli et al. 2019; Breivik et al. 2020; Bavera et al. 2020), dynamical formation through multibody interactions in star clusters (from low-mass stars to large nuclear star cluster;

Portegies Zwart & McMillan 2000; Rodriguez et al. 2015, 2016; Rodriguez & Loeb 2018; Di Carlo et al. 2019; Antonini & Gieles 2020; Santoliquido et al. 2021; Kremer et al. 2020) or AGN disks (Bartos et al. 2017; Yi & Cheng 2019; Yang et al. 2019, 2020; Gröbner et al. 2020; Samsing et al. 2020; Tagawa et al. 2020a, 2020b, 2021), Population III (Pop III) stars (Kinugawa et al. 2014, 2016; Hartwig et al. 2016; Belczynski et al. 2017), or primordial BHs (Carr & Hawking 1974; Bird et al. 2016; Sasaki et al. 2016; Ali-Haïmoud et al. 2017; Clesse & García-Bellido 2017; Raidal et al. 2017, 2019; Boehm et al. 2020; Hall et al. 2020; Wong et al. 2021a).

For simplicity, in this paper, we use galactic fields and globular clusters as the only main populations at low redshift and Pop III stars as the only high-redshift channel. The analysis can be easily extended to even more populations at the price of an increased computational cost.

Hereafter, we label the BBHs in the three formation channels as *field binaries*, *cluster binaries*, and *Pop III binaries*. Since an astrophysical BH is a remnant of stellar collapse, the merger rate history of each channel is correlated with the SFR and the time delay from binary formation to merger. Cluster and field binaries consist of BH remnants left over from Population I/II stars, whose corresponding SFR peaks at late times: $z \sim 3$ (Madau & Dickinson 2014; Vangioni et al. 2015). Accounting for the typical time delay between binary formation and merger ($\sim 10 \text{ Myr}$ to $\sim 10 \text{ Gyr}$), their merger rates are expected to peak at around $z \sim 2$ (Dominik et al. 2013; Belczynski et al. 2016; Rodriguez & Loeb 2018; Mapelli et al. 2019).

Pop III stars are instead formed at early times, $z \gtrsim 10$, from primordial gas clouds at extremely low metallicity (de Souza et al. 2011; Vangioni et al. 2015). The “metal-free” environment reduces the stellar wind mass loss during the binary evolution (Baraffe et al. 2001) so that Pop III stars might be more massive than later stellar populations. Eventually, heavy BH remnants are left behind that merge in a short timescale, resulting in a merger rate density that could peak at around $z \sim 10$ (Kinugawa et al. 2014, 2016; Belczynski et al. 2016; Hartwig et al. 2016).

The fact that different formation channels result in different merger rate distributions as a function of redshift, especially for Pop III remnants, can be exploited to infer the properties of BBH populations solely based on the redshift distribution of the detected sources. More elaborate tests can be envisaged that also rely on other distinguishing features, e.g., masses, spins, or eccentricity of the sources. In this study, we will show that tests based on the redshift distribution alone can already provide significant constraints, while also having the benefit of being model-independent, at least in some of the implementations we demonstrate below. This seems particularly desirable, since the true distribution of intrinsic parameters such as masses and spins is highly uncertain, especially for Pop III remnants.

In Figure 1, we show the “true” merger rate densities of three formation channels we use in this study and focus on key features of their shapes (we will discuss the branching ratios, i.e., the relative scale, later). The rate densities of field (orange), cluster (blue), and Pop III (green) binaries are phenomenological fits (details in Appendix C, Equations (C1)–(C3)) of the population synthesis simulation from Belczynski et al. (2016), Rodriguez & Loeb (2018), and Belczynski et al. (2017), respectively. We notice that the high-redshift tail of the cluster merger rate density is much steeper than that of the field

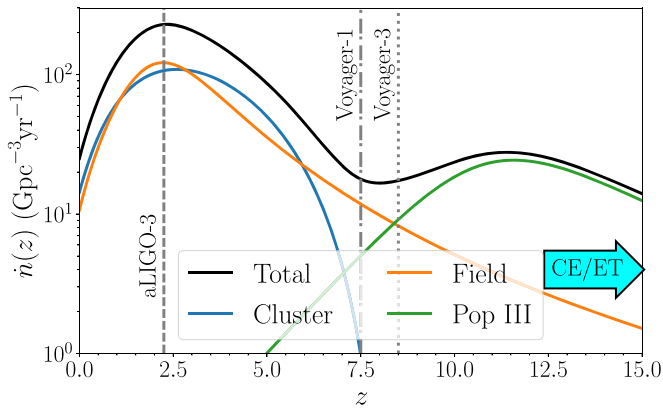


Figure 1. Merger rate densities of field (orange), cluster (blue), and Pop III (green) binaries, together with the overall merger rate (black), given by the sum of the three populations. For the purposes of this plot, field and cluster merger rate densities are normalized such that they produce the same number of binaries up to z of 15. The Pop III merger rate density is scaled so that its peak has an amplitude of $1/10$ relative to the peak of the field and cluster merger rate densities. The vertical lines indicate the detector horizons, z_h , to BBHs with total masses (in the comoving frame) $\leq 100 M_\odot$ in a network of three advanced detectors ($z_h \sim 2.25$), a single Voyager (Adhikari et al. 2019; $z_h \sim 8.5$), and a network of three Voyager-like detectors ($z_h \sim 12.1$; Hall & Evans 2019). The S/N threshold for detection is set to be 8 for a single detector and 12 for a detector network.

binaries. This is largely due to the choice of model; the cluster merger rates are based on the model of globular cluster formation from El-Badry et al. (2019), which goes to zero at $z \sim 10$. That, combined with the delay between cluster formation and BBH mergers (since BHs in clusters can only merge after the cluster has formed *and* the BHs have sunk to the center due to dynamical friction, a process that can take ~ 100 Myr; e.g., Morscher et al. 2015), causes a steeper slope in the merger rate at high z . The field and cluster merger rate densities peak at similar values, $z \sim 2.2$ and 2.6 , respectively, whereas the Pop III merger rate density peaks much later, at $z \sim 11.6$.

The vertical lines in Figure 1 report the horizon of future ground-based detector networks. Advanced detector networks can observe BBHs up to the low-redshift peak of the merger rate densities of the two dominating channels, fields, and clusters. However, as the plot shows, for $z \lesssim 2$, the merger rate densities of both field and cluster binaries are quite similar. Hence, advanced detectors are unlikely to be able to disentangle the two channels using only redshift information (as mentioned above, one can use other features, at the price of making the analysis more model-dependent). The situation improves with a single Voyager detector (“Voyager-1” line), which can access most of the field and cluster binaries up to $z \lesssim 8$ and therefore exploit the expected difference in their merger rate after the peak to characterize the two channels. A network of three Voyager-like detectors (“Voyager-3” line) can extend the horizon to a redshift where the contribution to the total merger rate of the field and the Pop III channel might become comparable. However, it is only with 3G detectors that one can access the peak of the merger rate from Pop III. In fact, the horizon of CE and ET to heavy BBHs is outside of the range of Figure 1 (as indicated by the cyan arrow in the bottom right corner), at $z \sim 100$. As we will show in the following sections, the fact that the horizon of 3G detectors extends well beyond the expected peak of Pop III mergers allows for both

modeled and unmodeled tests of the existence of such a subpopulation.

3. Results

In this work, we follow two approaches to measure the comoving-frame merger rate density dR/dz : (i) a unmodeled approach that utilizes Gaussian process regression (GPR) to infer dR/dz as a piecewise function over several redshift bins (Mandel et al. 2017) and (ii) a modeled approach in which we use phenomenological models for the various subpopulations (Farr et al. 2015; Vitale et al. 2019). In both cases, we use a hierarchical Bayesian inference framework (Farr et al. 2015; Mandel et al. 2019; Thrane & Talbot 2019; Wysocki et al. 2019; Vitale 2020) to measure the parameters of the population(s). More details are provided in Appendix A. Details about the implementation of the GPR analysis can be found in Appendix B, whereas Appendix C reports the functional forms of the modeled populations. The priors used in the analysis are documented in Appendix E.

To study how well the models can identify the Pop III subpopulation, we perform a mock-data challenge by simulating 18 different universes, which contain 2 months worth of BBH data with a majority of cluster or field binaries. The detailed setup of the simulations can be found in Appendix D.

In the following, we will focus on the measurement of the volumetric merger rate density, $\dot{n}(z) \equiv dR/dV_c$, rather than R itself. (We will use an index to indicate the volumetric merger rate in a specific channel, e.g., $\dot{n}_{\text{III}}(z)$ for the volumetric merger rate in the Pop III channel. Here “F” will indicate the field channel and “G” the globular cluster channel.) We will also report the branching ratios between the channels. Here f_{III} will indicate the fraction of Pop III mergers over the total, whereas f_G will indicate the fraction of cluster binaries over the sum of field and cluster binaries.

Our modeled approach naturally provides more information about the characteristic parameters of each channel and their correlations. Those are discussed in Appendix F.

3.1. Unmodeled Analysis

Figure 2 shows our inference on the volumetric merger rate \dot{n} obtained with the unmodeled GPR approach. The gray bands report the 68% and 95% credible intervals for the universes with (right panel) and without (left panel) Pop III binaries. The colored lines show the true volumetric merger rate of the individual populations. For both of the panels, the true branching ratio between field and cluster binaries is $f_G = 0.5$. We find that the true \dot{n} values (black solid lines) lie within the 95% credible intervals in both cases. While the relative uncertainty on \dot{n} is at a percent level at $z \lesssim 6$, it increases to $\mathcal{O}(100\%)$ at $z \gtrsim 8$. This is because (i) the S/N of each source decreases with the distance and (ii) the number of sources in each redshift bin is decreasing as the differential comoving volume shrinks at earlier times in the history of the universe.

Perhaps the most attractive feature of the unmodeled analysis is that we can find some evidence for the presence of a high-redshift subpopulation, even without strong modeling. The simplest way of doing this is to look for local peak(s) in \dot{n} . At the very minimum, we would expect to find evidence for the “main” peak at $z \sim 2$ arising from the merger in fields and clusters, while high-redshift peaks would be indicative of a different subpopulation.

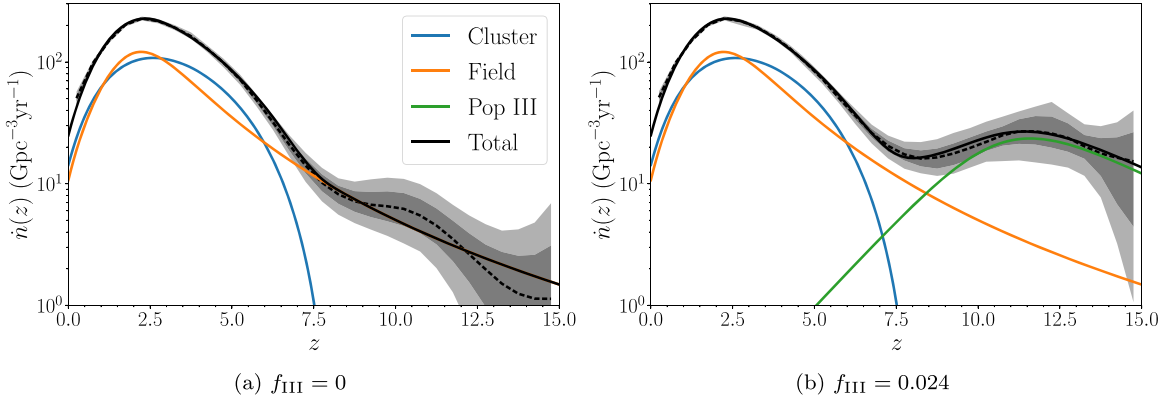


Figure 2. Reconstruction of \dot{n} for the $\tilde{f}_G = 0.5$ universes with (right panel) and without (left panel) Pop III binaries using GPR. The gray bands and dashed line show the 68% (darker color) and 95% (lighter color) credible intervals and the median of the recovered \dot{n} , respectively. The black, orange, blue, and green solid lines are the fiducial \dot{n} , \dot{n}_F , \dot{n}_G , and \dot{n}_{III} , respectively. Since we cannot model each subpopulation with the nonparametric approach, no hyperposterior can be drawn for each branch.

We implement a peak finder algorithm simply by asking the first derivative of \dot{n} to be zero and the second to be negative: $d\dot{n}/dz = 0$ and $d^2\dot{n}/dz^2 < 0$. Some care is required to avoid false positives due to natural oscillations in the results of the GRP that are not due to astrophysical maxima (or minima) but only to the underlying Gaussian process. These are particularly visible at high redshifts in Figure 2(a). To mitigate the effect of these fluctuations, we require the height of any high-redshift peaks to be at least 1/10 of the height of the low-redshift peak, as well as an intrapeak separation larger than $\Delta z = 1$. These requirements are based on the expected excess of Pop III, as discussed in Appendix D, and arguably represent the only modeling involved in the GRP approach that we describe.

With these two restrictions, we count the number of peaks N_{peak} for each \dot{n} sample of the GRP in every simulated universe. The results are shown in Figure 3 as a function of the true branching ratio cluster/field. For the universes without Pop III binaries, we recover a single peak, as expected, with $>99\%$ probability (purple histograms). This implies the nonexistence of a secondary peak whose relative height is $\geq 10\%$ of the primary peak. On the other hand, the true value for the number of peaks, $N_{\text{peak}} = 2$, is found at $\geq 90\%$ credibility for the universes with Pop III binaries (yellow histograms).

We observe that in the universes with Pop III binaries, the posterior on the number of peaks has a secondary mode at $N_{\text{peak}} = 3$ for $\tilde{f}_G \lesssim 0.5$. We explain this as follows: for $\tilde{f}_G \lesssim 0.5$, the field binaries are the dominating channel and, as is clear in Figure 2, produce a flatter high-redshift tail than the cluster channel. Hence, it is easier to produce multiple peaks due to fluctuation and induce a leakage to $N_{\text{peak}} \geq 3$. On the other hand, when $\tilde{f}_G \gtrsim 0.5$, the cluster binaries are dominating and do not contribute to the merger rate at $z \gtrsim 8$, where Pop III becomes the only source of BBHs, which makes the high-redshift peak narrower and hence easier to reveal. But the Poisson fluctuation of the high-redshift bins in dR/dz may still lead to an underestimation of the relative height below our 10% threshold, inducing a small contamination at $N_{\text{peak}} = 1$. We note that the above trend is subject to the model uncertainty of our chosen simulation data in the high-redshift region.

This method also allows for measuring the location(s) of the peak(s), which would be useful to understand the population properties. For instance, the shift of the primary peak relative to the SFR could inform the typical time delay to merger and a hint of metallicity evolution (Chruslinska et al. 2019; Santoliquido et al. 2021). In addition, constraining the

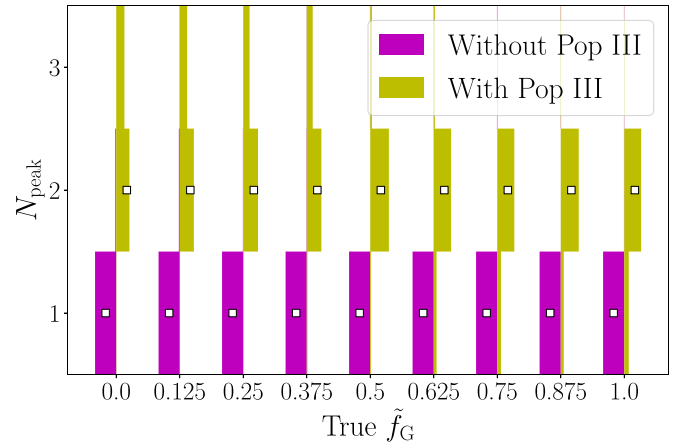


Figure 3. Posterior distributions of the N_{peak} of \dot{n} for all 18 universes. Since N_{peak} is a discrete measure, the distributions are represented by histograms. For the universes with (yellow) and without (purple) Pop III binaries, the true N_{peak} values are 2 and 1, respectively.

high-redshift peak to $z \gtrsim 8$ would provide support for the existence of Pop III binaries.

We first show the inferred distribution of the low-redshift peak, z_l , for all universes in Figure 4. All measurements of z_l constrain the low-redshift peaks to $z < 3$, with 95% credible interval uncertainties of $\sim 40\%$. The true values are contained within the uncertainty.

Next, we look at the measurements of the high-redshift peak's location z_h for the universes with Pop III binaries, as shown by the orange violins in Figure 5. In all cases, the true value $\hat{z}_h = 11.6$ lies within the 95% credible intervals. The lower bound of the credible interval is above $z \sim 7$ for all values of \tilde{f}_G , indicating that one can confidently place the secondary peak at a redshift much larger than where the star formation peaks. The widths of the credible intervals decrease from $\sim 50\%$ to $\sim 25\%$ when \tilde{f}_G increases from zero to 1. This may again be explained by the steeper redshift tail in the cluster population, which makes the Pop III peak easier to resolve.

3.2. Phenomenological Analysis

Having shown how a simple nonparametric model can already provide insight into the existence of a high-redshift population of BBHs, we now repeat the hierarchical inference using the phenomenological model described in Appendix C.

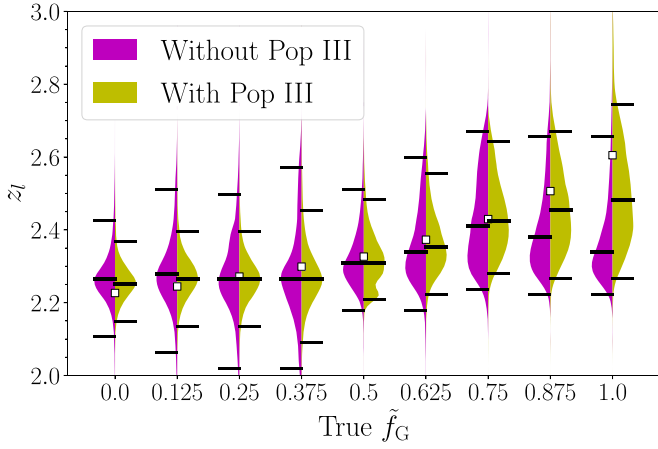


Figure 4. Hyperposterior of z_l for all universes, split into two categories: with (yellow) and without (purple) Pop III binaries. In each half-leaf, the upper and lower black dashes mark the 95% credible interval, and the middle black dash locates the median. The squares indicate the true values of z_l .

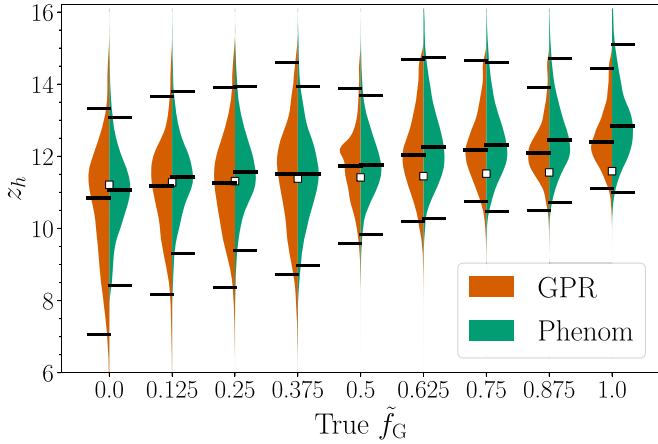


Figure 5. Hyperposterior of z_h for the nine universes with Pop III binaries, conditioned with $\dot{n}(z_h) \geq 0.1\dot{n}(z_l)$ inferred by the GPR model (orange) and the phenomenological (Phenom) model (green). Other plot settings are the same as in Figure 4.

We start by showing the posteriors on the peak of the merger rate density for the Pop III BBHs, this time obtained as one of the parameters of the phenomenological Pop III model,⁷ in Figure 5 (green violins). Remembering that the orange violins in the same plot report the measurement we obtained with the GPR approach, we find that the two methods yield very consistent results, with the widths of the 95% credible intervals varying by $\sim 10\%$ at most. The consistency between the two approaches highlights the promise of the nonparametric approach in revealing the existence and location of a high-redshift population. However, the phenomenological model directly describes the morphology of each subpopulation and thus allows for extracting information about each individual population, which cannot be accessed with the nonparametric approach.

In Figure 6, we show the inferred \dot{n} for the simulated $\tilde{f}_G = 0.5$ universes with (right panel) and without (left panel) Pop III binaries.⁸ For each population, the solid line represents the true merger rate, whereas the dashed line and colored band represent the median and 68%/95% credible intervals.

The total \dot{n} (black band) can be well constrained within a few percent level up to $z \sim 6$. For $f_{\text{III}} = 0$, the relative uncertainty rises to $\sim 100\%$ at $z \gtrsim 10$. Even at low redshift, the uncertainty of \dot{n}_F (orange band) and \dot{n}_G (blue band) is about 50%, ~ 10 times larger than that of the total rate, \dot{n} . This is because the morphology of \dot{n}_F and \dot{n}_G is similar at $z \lesssim 3$, where most of the BBHs can be detected with a precise distance measurement. Conversely, \dot{n}_F and \dot{n}_G are easier to distinguish at $z \gtrsim 5$, where, as discussed before, \dot{n}_G is declining more rapidly than \dot{n}_F , which instead has a long tail at $z \gtrsim 8$. Overall, the similarity in the morphology of the low-redshift volumetric merger rate of the two dominating channels induces degeneracies, and hence boosts uncertainties, in the individual merger rates, \dot{n}_F and \dot{n}_G .

Considering now the universe with $f_{\text{III}} = 0.024$ (right panel), we find that rate of the Pop III curve (green band) near its peak at $z \sim 12$ can be measured with a relative uncertainty of $\sim 50\%$, while the uncertainty of other channels remains similar to the universe with $f_{\text{III}} = 0$.

We compare the phenomenological recovery of the total \dot{n} to the GPR recovery (Figure 2) for the same universes and find that the typical uncertainty of \dot{n} is smaller by a factor of ~ 2 . This is not surprising, since the phenomenological approach uses models for the subpopulations, which inform the recovery of the overall merger rate. Naturally, the price to pay for the improved precision is to have made the results depend on the goodness of the models.

It is worth looking at the correlations between the hyperparameters of the various subpopulations. Some correlation should be expected, since, for example, the number of sources at high redshift might be potentially explained either by the model with a larger fraction of field binaries, which have a fat high-redshift tail, or by binaries in the Pop III channel. In Figure 7, we show the marginalized 2D contours of the $(\tilde{f}_G, f_{\text{III}})$ pair for the universes $\tilde{f}_G = 0.5$ with (yellow) and without (purple) Pop III. A positive correlation between the two parameters is clearly visible. This is caused by the partial model degeneracy between \dot{n}_F and \dot{n}_{III} . This goes exactly in the direction one would expect; underestimating f_{III} means that the model must increase the number of field binaries to account at least partially for the high-redshift binaries. But if the number of field binaries increases, \tilde{f}_G must decrease.

The partial correlation between \dot{n}_F and \dot{n}_{III} manifests itself in two other interesting ways. First, we observe an increase in the uncertainty of \tilde{f}_G when Pop III mergers are present. In Figure 8, we show violin plots for the marginalized \tilde{f}_G posteriors at different true \tilde{f}_G values. The yellow and purple violins correspond to the universes with and without Pop III binaries, respectively. While the true values lie inside the 95% credible interval in all cases, the uncertainties increase by $\sim 10\%$ for the universes with Pop III binaries.

Second, the uncertainty in f_{III} decreases as \tilde{f}_G increases. Figure 9 is a plot similar to Figure 8 but showing the marginalized f_{III} posteriors in different universes. When Pop III binaries are present, the uncertainty stays roughly constant, $\Delta f_{\text{III}} \sim 0.1$, up to $\tilde{f}_G \lesssim 0.5$, after which it drops gradually to $\Delta f_{\text{III}} \sim 0.05$ at $\tilde{f}_G = 1$. A similar trend is observed when no Pop III binaries exist; the uncertainty drops from $\sim 2.5\%$ to $\lesssim 0.1\%$. This is because \dot{n}_F has a longer tail in the high redshift $z \gtrsim 8$ and is easier to confuse with a small excess of Pop III.

⁷ That is, z_{III} of the Pop III model described in Appendix C.

⁸ These are the same two universes as in Figure 2.

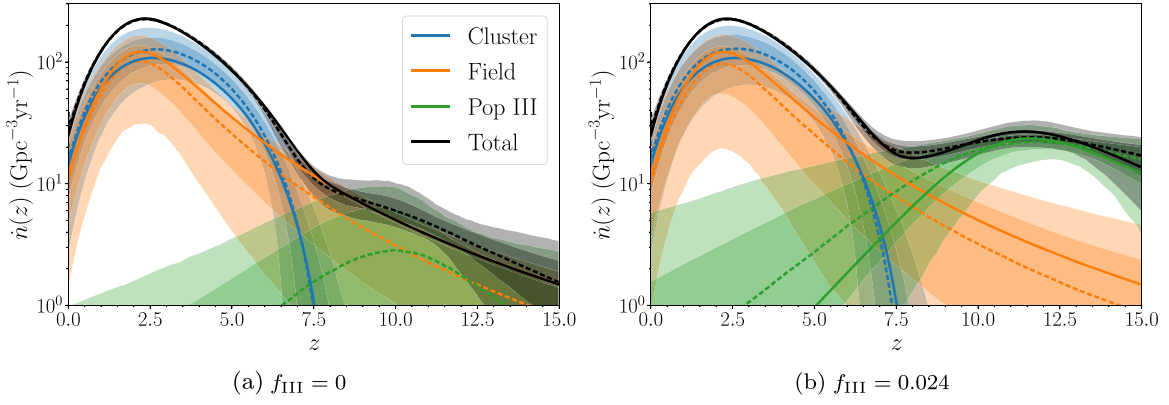


Figure 6. Reconstruction of merger rate densities for the $\tilde{f}_G = 0.5$ universes with (right panel) and without (left panel) Pop III binaries using phenomenological models. The orange, blue, green, and black dashed lines are the medians of the recovered \dot{n}_F , \dot{n}_G , \dot{n}_{III} , and \dot{n} , respectively. The corresponding colored bands are the 68% (darker colors) and 95% (lighter colors) credible intervals of the reconstruction. The true merger rate densities are shown as the dashed lines of the same colors. The green solid line is invisible, since there are no Pop III binaries in this universe.

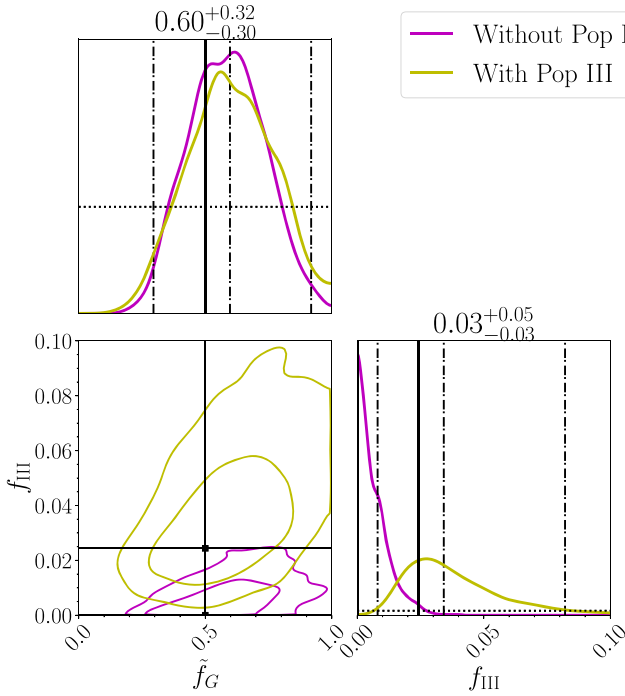


Figure 7. Hyperposterior of the population fractions, $(\tilde{f}_G, f_{\text{III}})$, for the universe with Pop III binaries $(\tilde{f}_G, f_{\text{III}}) = (0.5, 0.024)$ (yellow). For each marginalized 1D posterior (purple solid line in each diagonal slot), the left and right black dashed-dotted lines mark the 95% highest posterior density credible interval, the middle black dashed-dotted line locates the median, and the black dotted line shows the prior. The numerical values of the median and 95% credible intervals are reported above the diagonal slots. The off-diagonal slots show the marginalized 2D posteriors, with the contours representing the 68% and 95% credible intervals. The black markers and solid lines indicate the true values, which lie within the 68% credible interval. As a comparison, we overlay the same hyperposterior for the universe without Pop III binaries $(\tilde{f}_G, f_{\text{III}}) = (0.5, 0)$ (purple), whose 95% credible intervals and median values are not shown.

4. Discussions and Conclusions

In this paper, we have shown that observations made by a network of 3G detectors can be used to infer the properties of different BBH populations using redshift-only information. The larger horizon of a 3G detector network allows for accessing thousands of BBHs per month up to $z \sim 15$, which is necessary to resolve the excess of high-redshift ($z \gtrsim 8$) BBHs originating

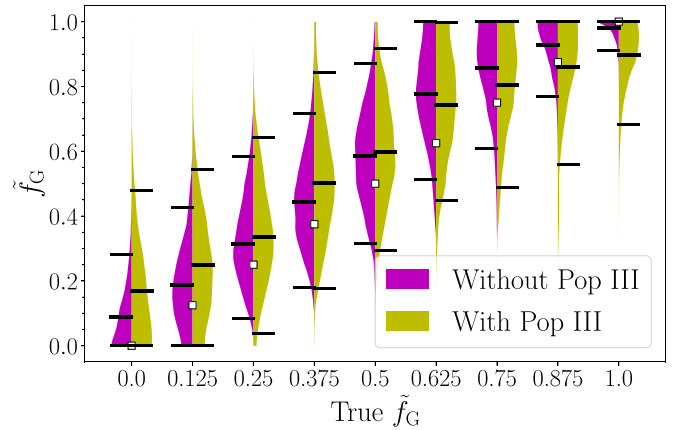


Figure 8. Marginalized hyperposteriors of \tilde{f}_G for all 18 universes. The plot setting is the same as in Figure 4.

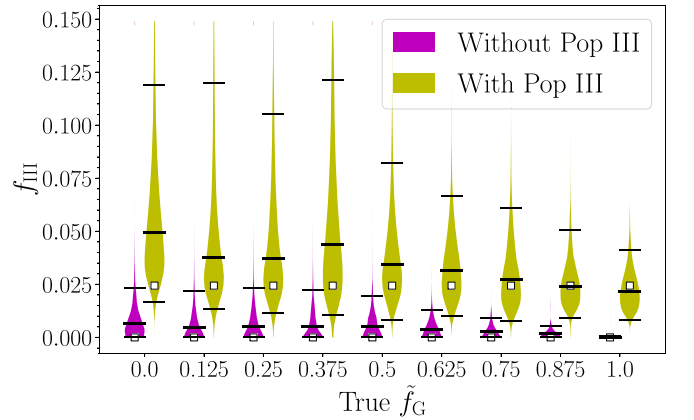


Figure 9. Marginalized hyperposteriors of f_{III} for all 18 universes. The plot setting is the same as in Figure 4.

from Pop III stars. We consider $\sim 16,000$ binaries, roughly corresponding to 2 months of data, and multiple values of the branching ratio between binary formation in galactic fields and globular clusters. For every value of this branching ratio, we analyzed both a case where a few hundred Pop III BBHs are present and one where they do not exist.

First, we consider a hierarchical inference approach based on a nonparametric reconstruction of the total volumetric merger

rate density \dot{n} . We look for local peaks in the reconstructed total merger rate and extract limited but useful information about the high-redshift population. By requiring that a possible high-redshift peak have an amplitude of at least 1/10 of the low-redshift peak, we find evidence for the presence of a high-redshift peak when Pop III binaries are included and constrain its position to be in the range $7 \leq z_h \leq 15$ for various mixing fractions between field and cluster binaries. Using the same approach, we rule out the existence of secondary peak structure if there were no Pop III binaries. This minimally modeled measurement of the position of a high-redshift peak (or lack thereof) in the total binary merger rate might, with some models, be translated into a measurement or an upper limit on the abundance of Pop III stars. With a similar approach, we are able to measure the position of a low-redshift peak, which might be used to investigate typical time delays between star formation and mergers.

Then, we considered a modeled analysis where a phenomenological model exists for each of the three subpopulations, which are characterized by a set of unknown hyperparameters measured from the data together with the (unknown) branching ratios. Among the most remarkable results, we found that, irrespective of the true value of the relative abundances of field and cluster binaries, the Pop III fraction can be constrained to be $f_{\text{III}} \gtrsim 0.01$ ($f_{\text{III}} \lesssim 0.02$) at 95% credibility for the universes that have (do not have) Pop III binaries. In both cases, the branching ratio between field and cluster binaries can be measured with better than $\sim 100\%$ uncertainty (95% credible interval). The precision of the measurement of Pop III mainly depends on the morphology of the merger rate densities of the dominating channels in the high-redshift region. If the dominating channels predict a shallower declining slope at high redshift, an eventual contribution to the high-redshift merger rate from Pop III is less distinctive, introducing correlations with the dominating channels.

Some studies suggest that Pop III might contribute to a nonnegligible fraction of the merger rate in the local universe (Hartwig et al. 2016; Liu & Bromm 2020a) or even a secondary peak in the low redshift $z \sim 2$ due to different formation scenarios (Kinugawa et al. 2020; Liu & Bromm 2020b). If this additional low-redshift peak exists, it will make the Pop III subpopulation more distinguishable while degrading the measurements of branching ratios, owing to extra degeneracies in the low-redshift regime.

We emphasize that our analysis is only assuming two months worth of data. A back-of-the-envelope calculation assuming that the statistical uncertainty shrinks like $1/\sqrt{N}$ would imply a factor of ~ 5 improvement over the results we present here after 5 yr of data. In that scenario, the phenomenological approach could identify a fraction of Pop III mergers as small as $f_{\text{III}} \sim 0.5\%$. However, as stressed multiple times in this work, the phenomenological inference requires reliable models for the merger rate of the various formation channels and will yield results that are as good as the models. On the other hand, the model-independent approach, though intrinsically less precise, has the attractive feature of not requiring any specific modeling of the underlying subpopulation. In this analysis, we used a three-detector network. A smaller network would lead to worse redshift measurements for individual sources and hence yield worse statistical uncertainties than reported in this paper. However, this can be compensated for by a longer observation time.

In this work, we have only considered three subpopulations: the galactic field and cluster binaries and high-redshift Pop III binaries. As mentioned above, many other channels have been proposed and can plausibly contribute a sizable fraction of the total rate. Our analysis can be trivially extended to include these and other subpopulations at the price of increasing computational cost and correlations and potentially degrading the measurement of some of the parameters. On the other hand, most of these different channels predict distinctive features in the BBHs they produce besides their redshift distribution, for example, masses, spins, and eccentricity (Dominik et al. 2012, 2013, 2015; de Mink & Belczynski 2015; Rodriguez et al. 2015, 2016; Belczynski et al. 2016; Bartos et al. 2017; O’Shaughnessy et al. 2017; Raidal et al. 2017, 2019; Stevenson et al. 2017; Vitale et al. 2017; Rodriguez & Loeb 2018; Di Carlo et al. 2019; Mapelli et al. 2019; Yang et al. 2019; Yi & Cheng 2019; Antonini & Gieles 2020; Biscoveanu et al. 2020; Breivik et al. 2020; Gröbner et al. 2020; Kremer et al. 2020; Samsing et al. 2020; Santoliquido et al. 2021; Yang et al. 2020; Tagawa et al. 2020a, 2020b, 2021). Including these features can enhance the precision of multipopulation inference, help break degeneracy between population models, and improve the understanding of each formation channel. We leave this extension of multidimensional BBH parameters in the 3G era to a future work.

The authors would like to thank Emanuele Berti, Hsin-Yu Chen, Carl Haster, and the LVK’s rate and population working group for fruitful discussions and comments. The authors also thank Katarina Martinovic, Carole Perigois and Tania Regimbau for cross-checking the validity of the Pop III phenomenological model. K.N. and S.V. acknowledge the support of the National Science Foundation through the NSF award PHY-1836814. K.N. and S.V. are members of the LIGO Laboratory. W.M.F. is funded by the Center for Computational Astrophysics at the Flatiron Institute, which is supported by the Simons Foundation. LIGO was constructed by the California Institute of Technology and Massachusetts Institute of Technology with funding from the National Science Foundation and operates under cooperative agreement PHY-1764464. This paper carries LIGO document No. LIGO-P2000540 and CE document No. CE-P2000007.

Appendix A Statistical Models

Here we briefly review the main statistical tool used in the analysis, i.e., the hierarchical Bayesian inference framework (Farr et al. 2015; Mandel et al. 2019; Thrane & Talbot 2019; Wysocki et al. 2019; Vitale 2020). We model the production mechanism of BBHs as an inhomogeneous Poisson process whose differential merger rate in the detector frame⁹ is given by

$$\frac{dR^d}{dz}(z|\mathbf{\Lambda}, R^d) = \frac{1}{1+z} \frac{dR}{dz}(z|\mathbf{\Lambda}, R), \quad (\text{A1})$$

where dR/dz is the differential merger rate in the comoving frame characterized by the “shape parameters” $\mathbf{\Lambda}$ and an overall normalization factor given by the total merger rate in the comoving frame $R = \int \frac{dR}{dz} dz$. The factor $1/(1+z)$

⁹ Here R and R^d measure mergers per unit time. The clocks used to measure the time interval, either the detector’s or the ones comoving with the sources, determine the frame in which the rate is calculated.

accounts for the cosmological time dilation effect so that the total merger rate in the detector frame is

$$R^d = \int \frac{dR^d}{dz} dz = \int \frac{1}{1+z} \frac{dR}{dz} dz. \quad (\text{A2})$$

The vector of shape parameters Λ contains the quantities that are used to model the underlying physical populations (see Section D).

One can write the hyperposterior of the population parameters Λ and R^d given a set of N_{obs} observations $\mathbf{d} \equiv \{d_i\}_{i=1}^{N_{\text{obs}}}$ as

$$\begin{aligned} p(\Lambda, R^d | \mathbf{d}) & \propto \left[\prod_{i=1}^{N_{\text{obs}}} T^d \int dz_i p(d_i | z_i) \frac{dR^d}{dz}(z_i | \Lambda, R^d) \right] e^{-R^d T^d} \\ & \times \pi(\Lambda, R^d) \\ & \simeq \left[\prod_{i=1}^{N_{\text{obs}}} T^d \frac{1}{M_i} \sum_{j=1}^{M_i} \frac{dR^d}{dz}(z_{ij} | \Lambda, R^d) \right] e^{-R^d T^d} \\ & \times \pi(\Lambda, R^d). \end{aligned} \quad (\text{A3})$$

In going from the second to the last line of Equation (A3), we have approximated the integrals with discrete sums. For the i th source, this amounts to calculating an average of the merger rate evaluated at the M_i points $\{z_{ij}\}_{j=1}^{M_i}$ drawn from the likelihood $p(d_i | z_i)$ of the i th source. In the third line, $\pi(\Lambda, R^d)$ is the hyperprior, and T^d is the experiment duration in the detector frame.

We find it more useful to quote the volumetric merger rate density, defined for the k th subpopulation as

$$\dot{n}_k(z) \equiv dR_k / dV_c,$$

where dV_c/dz is the differential comoving volume. Then, the merger rate history dR_k^d/dz in the detector frame as a function of redshift for the k th subpopulation is

$$\frac{dR_k^d}{dz}(z | \Lambda_k, R_k^d) = \frac{1}{1+z} \frac{dV_c}{dz} \dot{n}_k(z | \Lambda_k, R_k), \quad (\text{A4})$$

where the subscript k denotes the relevant quantities of the k th subpopulation.

The overall merger rate can be expressed as the sum of the individual merger rates of all P subpopulations ($P=3$ in our analysis), i.e.,

$$\frac{dR^d}{dz}(z | \Lambda, R^d) = \sum_k^P \frac{dR_k^d}{dz}(z | \Lambda_k, R_k^d), \quad (\text{A5})$$

where the vectors Λ and R^d contain all Λ_k and R_k^d , respectively. Since $\sum_k R_k = R$ and $\sum_k R_k^d = R^d$, we may rewrite Equation (A5) in terms of the branching ratios in the detector frame, i.e., the fraction of sources in each subpopulation, $f_k \equiv R_k^d / R^d$,

$$\frac{dR^d}{dz}(z | \Lambda, R^d) = R^d \sum_k^P f_k p_k^d(z | \Lambda_k), \quad (\text{A6})$$

where $p_k^d(z | \Lambda_k)$ is the normalized merger rate of the k th population in the detector frame, and the f_k are subject to the constraint $\sum_k f_k = 1$. Since we expect the fraction of Pop III binaries to be small, it is more convenient to introduce the fraction of cluster binaries over the sum of field and cluster binaries, $\tilde{f}_G \equiv f_G / (f_G + f_F)$.

Therefore, for the parameterized analysis, we model the merger rates of the three subpopulations in terms of several phenomenological parameters, which are treated as unknowns, together with the branching ratios (Appendix D). The total merger rate in Equation (A3) is thus calculated by adding up the contribution of each channel. On the other hand, in the unmodeled approach, we measure the overall $\frac{dR}{dz}(z | \Lambda, R)$ directly, without making any assumption about the individual subpopulations that might be contributing to it.

More details on the two approaches can be found in Appendices B and C, whereas the hyperpriors are described in Appendix E. Throughout the study, we assume Planck 15 cosmology (Ade et al. 2016).

Appendix B Gaussian Process Regression

This section provides details on the implementation of the GRP that we use to infer \dot{n} without assuming any specific functional form. We only require that dR/dz is sufficiently smooth such that dR/dz can be described by a piecewise-constant function over $W=30$ redshift bins, which are uniformly distributed in linear space in the range $0 \leq z \leq 15$. The merger rate dR/dz is thus written as

$$\frac{dR}{dz} = \begin{cases} \frac{\Delta R_1}{\Delta z_1} & 0 \leq z < z_1 \\ \dots & \\ \frac{\Delta R_i}{\Delta z_i} & z_{i-1} \leq z < z_i \\ \dots & \\ \frac{\Delta R_W}{\Delta z_W} & z_{W-1} \leq z < z_W \end{cases}, \quad (\text{B1})$$

where ΔR_i is the merger rate in the i th redshift bin $\Delta z_i \equiv z_i - z_{i-1} = 0.5$ so that $\sum_{i=1}^W (\Delta R_i) \equiv R$. To make the GPR more efficient, we infer dR/dz in natural-log space. Then, we apply a squared-exponential Gaussian process prior on $X_i \equiv \ln(\Delta R_i)$, with a covariance kernel

$$\begin{aligned} K_{ij} & \equiv \text{Cov}(X_i, X_j) \\ & = \sigma_X^2 \exp \left[-\frac{1}{2} \left(\frac{z_{i-1/2} - z_{j-1/2}}{l} \right)^2 \right], \end{aligned} \quad (\text{B2})$$

where $z_{i-1/2} = \frac{1}{2}(z_i - z_{i-1})$ is the midpoint of the i th redshift bin, σ_X^2 is the variance of $\{X_i\}$, and l is the correlation length in redshift space. The multivariate Gaussian process prior on the random variable vector $\mathbf{X} \equiv \{\ln(\Delta R_i)\}$ with a mean vector $\boldsymbol{\mu}_X$ and covariance matrix $\mathbf{K} \equiv \{K_{ij}\}$ is then

$$\mathcal{G}(\mathbf{X} | \boldsymbol{\mu}_X, \sigma_X, l) \equiv \mathcal{N}[\mathbf{X} | \boldsymbol{\mu}_X, \mathbf{K}(\sigma_X, l)]. \quad (\text{B3})$$

The kernel \mathbf{K} enforces the smoothness of dR/dz on scales that are comparable to or larger than l , which may be much larger than the bin spacing if the data support it, and prevents overfitting when W is large (Foreman-Mackey et al. 2014). To further enhance the sampling efficiency, we utilize the Cholesky factorization to decompose \mathbf{K} into a lower-triangular matrix \mathbf{L} , such that

$$\mathbf{X} \equiv \boldsymbol{\mu}_X + \mathbf{L}(\sigma_X, l) \boldsymbol{\eta} \quad (\text{B4})$$

follows the same Gaussian process prior \mathcal{G} by drawing $\boldsymbol{\eta}$ from a multivariate standard normal distribution. A common choice of $\boldsymbol{\mu}_X$ is a constant mean vector $\mu_X \mathbf{1}$. Since we know that dR/dz has a strong dependence of the redshifted differential comoving volume $dV_c/dz/(1+z)$, we further impose the mean of the Gaussian process prior to be the natural log of $dV_c/dz/(1+z)$ (normalized to N_{obs} within the comoving volume V_c and the observation time T) with a common shift $\Delta\mu_X$, i.e.,

$$\{\mu_{X,i}\} = \left\{ \ln \left(\frac{N_{\text{obs}}}{V_c T} \int_{z_{i-1}}^{z_i} \frac{1}{1+z} \frac{dV_c}{dz} dz \right) + \Delta\mu_X \right\}, \quad (\text{B5})$$

and we treat $\Delta\mu_X$, which is a single variable, as an additional parameter to include any possible fluctuation in the normalization R . We then obtain \dot{n} from dR/dz divided by the differential volume in each bin. All together, the $W+3=33$ hyperparameters in the GPR are thus

$$\Lambda_{\text{GPR}} = (\{\eta_i\}_{i=1}^W, \Delta\mu_X, \sigma_X, l). \quad (\text{B6})$$

Appendix C Phenomenological Models

Directly modeling the volumetric merger rate \dot{n} of a subpopulation as a function of astrophysical quantities, such as various distributions of initial stellar mass, the mass/radius of star clusters, BH natal kicks, or stellar metallicity, requires detailed stellar evolution or N -body simulations that are computationally expensive. To facilitate our analysis, we model the three formation channels phenomenologically. For the field, we follow the Madau–Dickinson functional form,¹⁰

$$\dot{n}_{\text{F}}(z|\alpha_{\text{F}}, \beta_{\text{F}}, C_{\text{F}}) \propto \frac{(1+z)^{\alpha_{\text{F}}}}{1 + \left(\frac{1+z}{C_{\text{F}}}\right)^{\beta_{\text{F}}}}, \quad (\text{C1})$$

where α_{F} , β_{F} , and C_{F} are unknown parameters that characterize the upward slope at $z \lesssim C_{\text{F}} - 1$, the downward slope at $z \gtrsim C_{\text{F}} - 1$, and the peak location of the volumetric merger rate density, respectively.

For cluster binaries, we describe the volumetric merger rate as a lognormal distribution in cosmic time, which we treat as a function of redshift,

$$\dot{n}_{\text{G}}(z|\mu_{\text{G}}, \sigma_{\text{G}}, t_{\text{G}}) \propto \text{LogNorm}(t(z) - t_{\text{G}}|\mu_{\text{G}}, \sigma_{\text{G}}), \quad (\text{C2})$$

where $t(z)$ is the cosmic time as a function of redshift, and LogNorm is the standard lognormal distribution of the argument $t - t_{\text{G}}$ parameterized by μ_{G} and σ_{G} . The additional parameter, t_{G} , is a reference time that marks the birth of the first cluster binaries.

For Pop III, we use the following functional form:

$$\dot{n}_{\text{III}}(z|a_{\text{III}}, b_{\text{III}}, z_{\text{III}}) \propto \frac{e^{a_{\text{III}}(z-z_{\text{III}})}}{b_{\text{III}} + a_{\text{III}}e^{(a_{\text{III}}+b_{\text{III}})(z-z_{\text{III}})}}, \quad (\text{C3})$$

where a_{III} , b_{III} , and z_{III} characterize the upward slope at $z < z_{\text{III}}$, the downward slope at $z > z_{\text{III}}$, and the peak location of the volumetric merger rate density, respectively.

¹⁰ Note that while we use the same form for the equation, we do not assume that the numerical coefficients are the same as the standard Madau–Dickinson SFR.

We have verified that these three phenomenological models can well fit the data from population synthesis analysis (Belczynski et al. 2016, 2017; Rodriguez & Loeb 2018) for the values of their arguments given in Equations (C1)–(C3).

We define the branching ratio between field and cluster binaries, \tilde{f}_{G} , implicitly through the equations

$$f_{\text{G}} \equiv \tilde{f}_{\text{G}}(1 - f_{\text{III}}), \quad (\text{C4})$$

$$f_{\text{F}} \equiv (1 - \tilde{f}_{\text{G}})(1 - f_{\text{III}}), \quad (\text{C5})$$

where $\{f_k\}$ are the original fractions of Equation (A6).

Therefore, there are a total of 12 hyperparameters in the phenomenological model:

$$\Lambda_{\text{PM}} = (\alpha_{\text{F}}, \beta_{\text{F}}, C_{\text{F}}, \mu_{\text{G}}, \sigma_{\text{G}}, t_{\text{G}}, a_{\text{III}}, b_{\text{III}}, z_{\text{III}}, \tilde{f}_{\text{G}}, f_{\text{III}}, R^d). \quad (\text{C6})$$

Appendix D Simulation Details

In this section, we describe how we prepare the simulated universes that will be analyzed with the methods described in the previous section.

First, we need to choose reference (i.e., “true”) merger rate densities that will be used to generate the redshift of the BBHs. We do so by means of the phenomenological curves in Equations (C1)–(C3). As described in Appendix C, these curves describe the morphology of each volumetric merger rate density and are parameterized by, e.g., the rising slope at low redshift, the declining slope at high redshift, and the redshift at which the merger rate peaks. The phenomenological curves are obtained by fitting Equations (C1)–(C3) to the simulation results available in the literature (Belczynski et al. 2016, 2017; Rodriguez & Loeb 2018). Specifically, we take the model-averaged simulation results of Belczynski et al. (2016) and Rodriguez & Loeb (2018) for field and cluster binaries, respectively, as well as the “FS1” model’s result of Belczynski et al. (2017) for Pop III binaries. We stress that our phenomenological fits include the effect of the time delay from binary formation to merger, as well as the impact of stellar metallicity on the binary evolution specified in the population synthesis analyses. In particular, this implies a quite remarkable fact: the same Madau–Dickinson function can be used to fit both the SFR (this is its normal use) and the merger rate density it implies for different values of its parameters.

We use the following numbers as the “true” values of each curve parameter when preparing our sources:

$$(\hat{\alpha}_{\text{F}}, \hat{\beta}_{\text{F}}, \hat{C}_{\text{F}}) = (2.57, 5.83, 3.36),$$

$$(\hat{\mu}_{\text{G}}, \hat{\sigma}_{\text{G}}, \hat{t}_{\text{G}}) = (1.63, 0.96, 0.66 \text{ Gyr}),$$

$$(\hat{a}_{\text{III}}, \hat{b}_{\text{III}}, \hat{z}_{\text{III}}) = (0.66, 0.3, 11.6).$$

While this fixes the true shape of the merger rate for each subpopulation, we still need to fix the amplitudes. We use nine different values of the relative merger rate between cluster and field binaries, \tilde{f}_{G} , equally spaced in the range from zero to 1. For each value of \tilde{f}_{G} , we consider two universes: one with and one without Pop III binaries.

Following the latest GWTC-2 result, we fix the local volumetric merger rate density to $\dot{n}(0) = 25 \text{ Gpc}^{-3}\text{yr}^{-1}$ (Abbott et al. 2020b). This yields $R_{\text{F}}^d + R_{\text{G}}^d \approx 8000 \text{ month}^{-1}$. In the

universes with Pop III binaries, the Pop III fraction $f_{\text{III}} \approx 0.024$ is chosen to generate an additional 200 sources month⁻¹ coming from the Pop III channel. This number is chosen such that the peak merger rate density of Pop III binaries is ~ 10 times smaller than the peak of the dominating channels. The nominal value of this peak, $\dot{n}_{\text{III}}(z_{\text{III}}) \approx 20 \text{ Gpc}^{-3}\text{yr}^{-1}$, is consistent with the comparison of the “FS1” model to the Population I/II field binaries in Belczynski et al. (2016). We stress that the current predictions for the Pop III merger rate span a few orders of magnitude in either direction relative to the one we are using (Kinugawa et al. 2014, 2016; Belczynski et al. 2016; Hartwig et al. 2016). This is because the formation efficiency of Pop III binaries greatly depends on the initial mass function of the Pop III stars and the distribution of the initial orbital separation (see Belczynski et al. 2016; Hartwig et al. 2016). Since \dot{n}_{III} declines rapidly at later cosmic time, it does not significantly contribute to $\dot{n}(0)$.

To ensure a reasonable measurement of luminosity distance, which typically requires three or more detectors, we choose a baseline detector network with one CE in Australia, one CE in the United States, and one ET in Europe (Vitale 2016; Vitale & Evans 2017; Vitale & Whittle 2018). Generally speaking, not all BBHs within the detector horizon can be detected with S/Ns over some thresholds, depending on their orientation and intrinsic parameters. This results in a Malmquist bias (Mandel et al. 2019; Vitale 2020). However, the efficiency only drops to 50% at $z \sim 20$ for a typical $30 M_{\odot}$ and $30 M_{\odot}$ BBH mass-pair. Therefore, we limit our analysis to the redshift range $0 \leq z \leq 15$ and neglect selection effect.

Finally, we simulate a month of data in the following way. We first draw the set of true redshifts, $\{z_{\text{true},i}\}$, from the “true” dR/dz in each universe. Then, for each $z_{\text{true},i}$, we obtain the observed redshift, $z_{\text{obs},i}$, by drawing a random variable from a mock-up single-event likelihood conditional on $z_{\text{true},i}$. Following Vitale et al. (2019), we approximate the likelihood for redshift as a lognormal distribution conditional on $z_{\text{true},i}$ with a standard deviation $\sigma_{\text{LN},i} = 0.017z_{\text{true},i}$. Finally, we draw 100 single-event likelihood samples conditional on $z_{\text{obs},i}$ with the same $\sigma_{\text{LN},i}$ as calculated previously. The second step is necessary in order to generate a scattering to the true value within the probable range of the single-event likelihood function. Otherwise, the alignment of the true value and the mean of the likelihood introduces systematic bias in the analysis.

To summarize, we generate 18 simulated universes. In all universes, we generate 16,000 (2 months worth of data) BBHs from field and cluster binaries with a given branching ratio \tilde{f}_{G} and add 400 more Pop III observations for the nine universes containing Pop III binaries.

Appendix E Hyperpriors

The priors of all of the Λ_{GPR} hyperparameters are tabulated in Table 1.

The priors of all of the Λ_{PM} hyperparameters are tabulated in Table 2. The choice of lognormal priors is made to restrict each model to always carrying a characteristic peak within the redshift range, rather than increasing or decreasing monotonically. The Gaussian prior and the domain of z_{III} ensure that the peak of \dot{n}_{III} lies at high redshift $z \geq 8$ and prevents \dot{n}_{III} from mimicking the two dominating channels that have peaks at low redshift $z \lesssim 3$.

Table 1
Hyperpriors for the GPR Model

$\Lambda_{\text{GPR},i}$	Prior Function	Prior Parameters	Domain
η_i	Normal	$(\mu_{\text{N}}, \sigma_{\text{N}}) = (0, 1)$	$(-\infty, +\infty)$
$\Delta\mu_X$	Normal	$(\mu_{\text{N}}, \sigma_{\text{N}}) = (0, 10)$	$(-\infty, +\infty)$
σ_X	Lognormal	$(\mu_{\text{LN}}, \sigma_{\text{LN}}) = (0, 4)$	$(0, +\infty)$
l	Lognormal	$(\mu_{\text{LN}}, \sigma_{\text{LN}}) = (0, \frac{1}{2}\ln(10))$	$(0, +\infty)$

Table 2
Hyperpriors for the Phenomenological Models

$\Lambda_{\text{PM},i}$	Prior Function	Prior Parameters	Domain
α_{F}	Lognormal	$(\mu_{\text{LN}}, \sigma_{\text{LN}}) = (\hat{\alpha}_{\text{F}}, 0.25)^{\text{a}}$	$(0, 10)$
β_{F}	Lognormal	$(\mu_{\text{LN}}, \sigma_{\text{LN}}) = (\hat{\beta}_{\text{F}}, 0.25)$	$(0, 20)$
C_{F}	Lognormal	$(\mu_{\text{LN}}, \sigma_{\text{LN}}) = (\hat{C}_{\text{F}}, 0.25)$	$(0, 6)$
μ_{G}	Lognormal	$(\mu_{\text{LN}}, \sigma_{\text{LN}}) = (\hat{\mu}_{\text{G}}, 0.25)$	$(0, 5)$
σ_{G}	Lognormal	$(\mu_{\text{LN}}, \sigma_{\text{LN}}) = (\hat{\sigma}_{\text{G}}, 0.25)$	$(0, 5)$
t_{G}	Lognormal	$(\mu_{\text{LN}}, \sigma_{\text{LN}}) = (\hat{t}_{\text{G}}, 0.25)$	$(0, 2.0)$
a_{III}	Lognormal	$(\mu_{\text{LN}}, \sigma_{\text{LN}}) = (\hat{a}_{\text{III}}, 0.5)$	$(0, 2)$
b_{III}	Lognormal	$(\mu_{\text{LN}}, \sigma_{\text{LN}}) = (\hat{b}_{\text{III}}, 1)$	$(0, 2)$
z_{III}	Normal	$(\mu_{\text{N}}, \sigma_{\text{N}}) = (\hat{z}_{\text{III}}, 2)^{\text{b}}$	$[8, 20]$
f_{III}	Uniform	...	$[0, 0.5]$
\tilde{f}_{G}	Uniform	...	$[0, 1.0]$
R^{d}	Half Cauchy	$\gamma_{\text{C}} = N_{\text{obs}}^{\text{c}}$	$[0, +\infty]$

^a Here μ_{LN} and σ_{LN} are the mean and standard deviation of the lognormal distribution, respectively.

^b Here μ_{N} and σ_{N} are the mean and standard deviation of the normal distribution, respectively.

^c Here γ_{C} is the scale parameter of the Cauchy distribution.

Appendix F Detailed Results from the Modeled Analysis

In this section, we report the population hyperposteriors for the modeled analysis, i.e., the posteriors of the variables that parameterize the individual subpopulations described in Appendix C, as well as the branching ratios.

First, we show the hyperposterior of the dominating channels’ parameters for the universe with $(\tilde{f}_{\text{G}}, f_{\text{III}}) = (0.5, 0)$ (the same as Figure 6(a)) in Figure 10. Most of the shape parameters are measured with $\sim 100\%$ uncertainty, e.g., $\tilde{f}_{\text{G}} = 0.59_{-0.27}^{+0.28}$. We note that there are a few interesting correlated pairs, such as $(t_{\text{G}}, \tilde{f}_{\text{G}})$ and $(t_{\text{G}}, \sigma_{\text{G}})$. Since t_{G} characterizes the starting time of the merging cluster binaries, an earlier t_{G} shifts the peak of the cluster population toward a higher redshift, where the cosmological volume is smaller. Hence, \tilde{f}_{G} needs to be larger to keep the same number of cluster binaries. On the other hand, a smaller t_{G} tends to shift the cluster population toward a lower redshift. Then, a larger σ_{G} is necessary to maintain a wide merger rate peak.

Next, we look at the hyperposterior of the Pop III merger rate parameters for the universe with $(\tilde{f}_{\text{G}}, f_{\text{III}}) = (0.5, 0)$ (the same as Figure 6), as shown by the purple contours in Figure 11. We are able to constrain $f_{\text{III}} \lesssim 0.02$. Both a_{III} and b_{III} are very close to their priors, which make sense, since f_{III} is small, which implies that no information about \dot{n}_{III} can be gained. On the other hand, the position of the peak, z_{III} , is shifted toward lower values relative to its prior to suppress the contribution from \dot{n}_{III} to the high-redshift total merger rate, which in this universe is entirely determined by the field binaries.

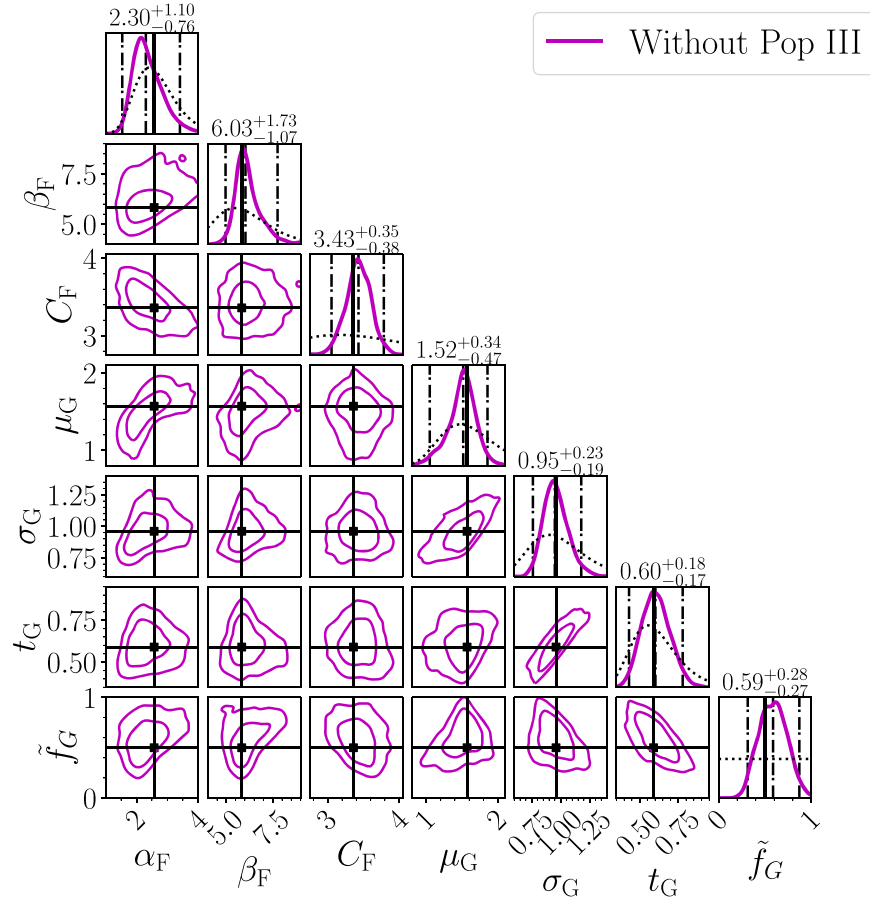


Figure 10. Hyperposterior of the dominating channels’ hyperparameters, $(\alpha_F, \beta_F, C_F, \mu_G, \sigma_G, t_G, \tilde{f}_G)$, for the universe with $(\tilde{f}_G, f_{\text{III}}) = (0.5, 0)$ (the same as Figure 6). For each marginalized 1D posterior (purple solid line in each diagonal slot), the left and right black dashed–dotted lines mark the 95% highest posterior density credible interval, the middle black dashed–dotted line locates the median, and the black dotted line shows the prior. The numerical values of the median values and 95% credible intervals are reported above the diagonal slots. The off-diagonal slots show the marginalized 2D posteriors, with the contours representing the 68% and 95% credible intervals. The black markers and solid lines indicate the true values, which lie within the 68% credible interval. The statistical behavior for the universe with Pop III is very similar.

For comparison, we also report the results for the universe with $f_{\text{III}} = 0.024$ (this is the same as in Figure 6(b)). In Figure 11, the yellow contours show the hyperposterior of the n_{III} parameters. While the shape parameters of a_{III} and b_{III} are still not well constrained, the peak $z_{\text{III}} = 11.75^{+1.92}_{-1.91}$ is measured

with $\sim 30\%$ relative uncertainty. Importantly, $f_{\text{III}} = 0$, i.e., the absence of a Pop III channel, is excluded from the 95% credible interval of the marginalized f_{III} posterior. This provides strong evidence of the existence of Pop III binaries in our simulated data.

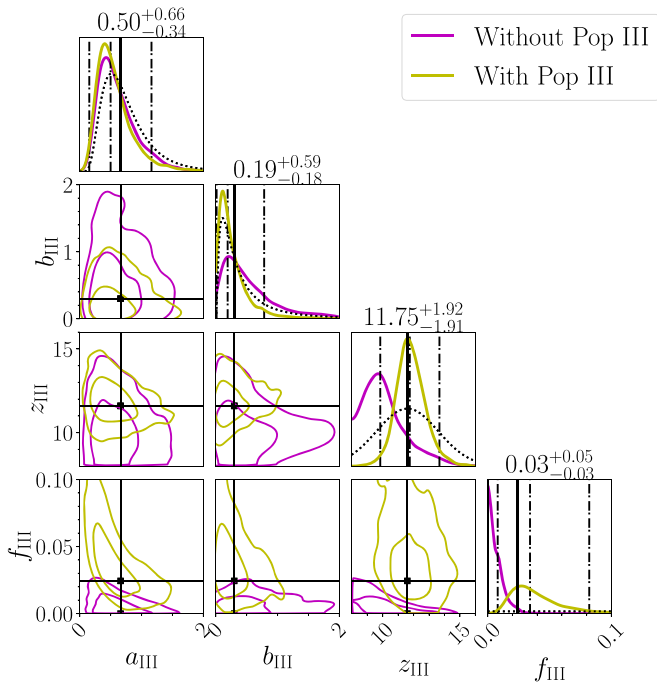


Figure 11. Hyperposterior of Pop III's hyperparameters, $(a_{\text{III}}, b_{\text{III}}, z_{\text{III}}, f_{\text{III}})$, for the universes $(\bar{f}_{\text{G}}, f_{\text{III}}) = (0.5, 0)$ (purple) and $(\bar{f}_{\text{G}}, f_{\text{III}}) = (0.5, 0.024)$ (yellow). For each marginalized 1D posterior (purple solid line in each diagonal slot), the left and right black dashed-dotted lines mark the 95% highest posterior density credible interval, the middle black dashed-dotted line locates the median, and the black dotted line shows the prior. The numerical values of the median values and 95% credible intervals are reported above the diagonal slots. The off-diagonal slots show the marginalized 2D posteriors, with the contours representing the 68% and 95% credible intervals. The black markers and solid lines indicate the true values, which lie within the 68% credible interval. Only the medians and 95% credible intervals for the universe with Pop III binaries (yellow) are indicated by the dashed-dotted lines and reported above the diagonal slots.

ORCID iDs

Ken K. Y. Ng <https://orcid.org/0000-0003-3896-2259>
 Salvatore Vitale <https://orcid.org/0000-0003-2700-0767>
 Will M. Farr <https://orcid.org/0000-0003-1540-8562>
 Carl L. Rodriguez <https://orcid.org/0000-0003-4175-8881>

References

Aasi, J., Abbott, B. P., Abbott, R., et al. 2015, *CQGra*, **32**, 074001
 Abbott, B. P., Abbott, R., Abbott, T. D., et al. 2016, *PhRvD*, **93**, 112004
 Abbott, B. P., Abbott, R., Abbott, T. D., et al. 2017, *CQGra*, **34**, 044001
 Abbott, B., Abbott, R., Abbott, T. D., et al. 2019a, *PhRvX*, **9**, 031040
 Abbott, B., Abbott, R., Abbott, T. D., et al. 2019b, *ApJL*, **882**, L24
 Abbott, R., Abbott, T. D., Abraham, S., et al. 2020a, arXiv:2010.14527
 Abbott, R., Abbott, T. D., Abraham, S., et al. 2020b, arXiv:2010.14533
 Abbott, R., Abbott, T. D., Abraham, S., et al. 2020c, *PhRvL*, **125**, 101102
 Abbott, R., Abbott, T. D., Abraham, S., et al. 2020d, *ApJL*, **900**, L13
 Acernese, F., Agathos, M., Agatsuma, K., et al. 2015, *CQGra*, **32**, 024001
 Ade, P., Aghanim, N., Arnaud, M., et al. 2016, *A&A*, **594**, A13
 Adhikari, R. X., Ajith, P., Chen, Y., et al. 2019, *CQGra*, **36**, 245010
 Ali-Haïmoud, Y., Kovetz, E. D., & Kamionkowski, M. 2017, *PhRvD*, **96**, 123523
 Amaro-Seoane, P., Audley, H., Babak, S., et al. 2017, arXiv:1702.00786
 Antonini, F., & Gieles, M. 2020, *PhRvD*, **102**, 123016
 Arvanitaki, A., Baryakhtar, M., Dimopoulos, S., Dubovsky, S., & Lasenby, R. 2017, *PhRvD*, **95**, 043001
 Aso, Y., Michimura, Y., Somiya, K., et al. 2013, *PhRvD*, **88**, 043007
 Baraffe, I., Heger, A., & Woosley, S. 2001, *ApJ*, **550**, 890
 Bartos, I., Kocsis, B., Haiman, Z., & Márka, S. 2017, *ApJ*, **835**, 165
 Bavera, S. S., Fragos, T., Qin, Y., et al. 2020, *A&A*, **635**, A97

Bavera, S. S., Fragos, T., Zevin, M., et al. 2021, *A&A*, **647**, A153
 Belczynski, K., Holz, D. E., Bulik, T., & O'Shaughnessy, R. 2016, *Natur*, **534**, 512
 Belczynski, K., Ryu, T., Perna, R., et al. 2017, *MNRAS*, **471**, 4702
 Belczynski, K., Klencki, J., Fields, C. E., et al. 2020, *A&A*, **636**, A104
 Bird, S., Cholis, I., Muñoz, J. B., et al. 2016, *PhRvL*, **116**, 201301
 Biscoveanu, S., Isi, M., Vitale, S., & Varma, V. 2020, *PhRvL*, **126**, 171103
 Boehm, C., Kobakhidze, A., O'Hare, C. A., Picker, Z. S., & Sakellariadou, M. 2020, arXiv:2008.10743
 Bouffanais, Y., Mapelli, M., Gerosa, D., et al. 2019, *ApJ*, **886**, 25
 Breivik, K., Coughlin, S., Zevin, M., et al. 2020, *ApJ*, **898**, 71
 Brito, R., Ghosh, S., Barausse, E., et al. 2017, *PhRvD*, **96**, 064050
 Broekgaard, F. S., Justham, S., de Mink, S. E., et al. 2019, *MNRAS*, **490**, 5228
 Callister, T., Farr, W., & Renzo, M. 2020a, arXiv:2011.09570
 Callister, T., Fishbach, M., Holz, D., & Farr, W. 2020b, *ApJL*, **896**, L32
 Carr, B. J., & Hawking, S. 1974, *MNRAS*, **168**, 399
 Chruslinska, M., Nelemans, G., & Belczynski, K. 2019, *MNRAS*, **482**, 5012
 Clesse, S., & García-Bellido, J. 2017, *PDU*, **15**, 142
 de Mink, S., & Belczynski, K. 2015, *ApJ*, **814**, 58
 de Souza, R. S., Yoshida, N., & Ioka, K. 2011, *A&A*, **533**, A32
 Di Carlo, U. N., Giacobbo, N., Mapelli, M., et al. 2019, *MNRAS*, **487**, 2947
 Doctor, Z., Wyosocki, D., O'Shaughnessy, R., Holz, D. E., & Farr, B. 2019, *ApJ*, **893**, 35
 Dominik, M., Belczynski, K., Fryer, C., et al. 2012, *ApJ*, **759**, 52
 Dominik, M., Belczynski, K., Fryer, C., et al. 2013, *ApJ*, **779**, 72
 Dominik, M., Berti, E., O'Shaughnessy, R., et al. 2015, *ApJ*, **806**, 263
 El-Badry, K., Quataert, E., Weisz, D. R., Choksi, N., & Boylan-Kolchin, M. 2019, *MNRAS*, **482**, 4528
 Farmer, R., Renzo, M., de Mink, S., Fishbach, M., & Justham, S. 2020, *ApJL*, **902**, L36
 Farr, B., Holz, D. E., & Farr, W. M. 2018, *ApJL*, **854**, L9
 Farr, W. M., Gair, J. R., Mandel, I., & Cutler, C. 2015, *PhRvD*, **91**, 023005
 Farr, W. M., Stevenson, S., Coleman Miller, M., et al. 2017, *Natur*, **548**, 426
 Fishbach, M., Farr, W. M., & Holz, D. E. 2020, *ApJL*, **891**, L31
 Fishbach, M., & Holz, D. E. 2017, *ApJL*, **851**, L25
 Fishbach, M., & Holz, D. E. 2020, *ApJL*, **904**, L26
 Fishbach, M., Holz, D. E., & Farr, B. 2017, *ApJL*, **840**, L24
 Fishbach, M., Holz, D. E., & Farr, W. M. 2018, *ApJL*, **863**, L41
 Foreman-Mackey, D., Hogg, D. W., & Morton, T. D. 2014, *ApJ*, **795**, 64
 Fragione, G., & Loeb, A. 2021, *MNRAS*, **502**, 3879
 Gaskin, J. A., Swartz, D. A., Vikhlinin, A., et al. 2019, *JATIS*, **5**, 021001
 Gerosa, D., & Berti, E. 2017, *PhRvD*, **95**, 124046
 Gerosa, D., Vitale, S., & Berti, E. 2020, *PhRvL*, **125**, 101103
 Greene, J. E., Strader, J., & Ho, L. C. 2020, *ARA&A*, **58**, 257
 Gröbner, M., Ishibashi, W., Tiwari, S., Haney, M., & Jetzer, P. 2020, *A&A*, **638**, A119
 Hall, A., Gow, A. D., & Byrnes, C. T. 2020, arXiv:2008.13704
 Hall, E. D., & Evans, M. 2019, *CQGra*, **36**, 225002
 Hartwig, T., Volonteri, M., Bromm, V., et al. 2016, *MNRAS*, **460**, L74
 Hütsi, G., Raidal, M., Vaskonen, V., & Veermäe, H. 2021, *JCAP*, **03**, 068
 Kimball, C., Berry, C. P., & Kalogera, V. 2019, *RNAAS*, **4**, 2
 Kimball, C., Talbot, C. L., Berry, C. P., et al. 2020a, *ApJ*, **900**, 177
 Kimball, C., Talbot, C., Berry, C. P., et al. 2020b, arXiv:2011.05332
 Kinugawa, T., Inayoshi, K., Hotokezaka, K., Nakauchi, D., & Nakamura, T. 2014, *MNRAS*, **442**, 2963
 Kinugawa, T., Miyamoto, A., Kanda, N., & Nakamura, T. 2016, *MNRAS*, **456**, 1093
 Kinugawa, T., Nakamura, T., & Nakano, H. 2021, *MNRAS Letters*, **501**, L49
 Kinugawa, T., Nakamura, T., & Nakano, H. 2020, *MNRAS*, **498**, 3946
 Kremer, K., Spera, M., Becker, D., et al. 2020, *ApJ*, **903**, 45
 Liu, B., & Bromm, V. 2020a, *MNRAS*, **495**, 2475
 Liu, B., & Bromm, V. 2020b, *ApJL*, **903**, L40
 Lower, M. E., Thrane, E., Lasky, P. D., & Smith, R. 2018, *PhRvD*, **98**, 083028
 Madau, P., & Dickinson, M. 2014, *ARA&A*, **52**, 415
 Maggiore, M., Van Den Broeck, C., Bartolo, N., et al. 2020, *JCAP*, **03**, 050
 Mandel, I., Farr, W. M., Colonna, A., et al. 2017, *MNRAS*, **465**, 3254
 Mandel, I., Farr, W. M., & Gair, J. R. 2019, *MNRAS*, **486**, 1086
 Mapelli, M., Giacobbo, N., Santoliquido, F., & Artale, M. C. 2019, *MNRAS*, **487**, 2
 McCuller, L., Whittle, C., Ganapathy, D., et al. 2020, *PhRvL*, **124**, 171102
 Miller, S., Callister, T. A., & Farr, W. 2020, *ApJ*, **895**, 128
 Morscher, M., Pattabiraman, B., Rodriguez, C., Rasio, F. A., & Umbreit, S. 2015, *ApJ*, **800**, 9
 Ng, K. K., Hannuksela, O. A., Vitale, S., & Li, T. G. 2021a, *PhRvD*, **103**, 063010

- Ng, K. K., Vitale, S., Hannuksela, O. A., & Li, T. G. 2021b, *PhRvL*, **126**, 151102
- O’Shaughnessy, R., Bellovary, J., Brooks, A., et al. 2017, *MNRAS*, **464**, 2831
- Portegies Zwart, S. F., & McMillan, S. L. W. 2000, *ApJL*, **528**, L17
- Punturo, M., Abernathy, M., Acernese, F., et al. 2010, *CQGra*, **27**, 194002
- Raidal, M., Spethmann, C., Vaskonen, V., & Veermäe, H. 2019, *JCAP*, **02**, 018
- Raidal, M., Vaskonen, V., & Veermäe, H. 2017, *JCAP*, **09**, 037
- Regimbau, T., Evans, M., Christensen, N., et al. 2017, *PhRvL*, **118**, 151105
- Reitze, D., Adhikari, R. X., Ballmer, S., et al. 2019, *BAAS*, **51**, 35
- Rodriguez, C. L., Chatterjee, S., & Rasio, F. A. 2016, *PhRvD*, **93**, 084029
- Rodriguez, C. L., & Loeb, A. 2018, *ApJL*, **866**, L5
- Rodriguez, C. L., Morscher, M., Pattabiraman, B., et al. 2015, *PhRvL*, **115**, 051101
- Romero-Shaw, I. M., Kremer, K., Lasky, P. D., Thrane, E., & Samsing, J. 2020, arXiv:2011.14541
- Roulet, J., Venumadhav, T., Zackay, B., Dai, L., & Zaldarriaga, M. 2020, *PhRvD*, **102**, 123022
- Safarzadeh, M., Berger, E., Ng, K. K.-Y., et al. 2019, *ApJL*, **878**, L13
- Safarzadeh, M., Farr, W. M., & Ramirez-Ruiz, E. 2020, *ApJ*, **894**, 129
- Samsing, J., Bartos, I., D’Orazio, D., et al. 2020, arXiv:2010.09765
- Santoliquido, F., Mapelli, M., Giacobbo, N., Bouffanais, Y., & Artale, M. C. 2021, *MNRAS*, **502**, 4877
- Sasaki, M., Suyama, T., Tanaka, T., & Yokoyama, S. 2016, *PhRvL*, **117**, 061101
- Stevenson, S., Ohme, F., & Fairhurst, S. 2015, *ApJ*, **810**, 58
- Stevenson, S., Vigna-Gómez, A., Mandel, I., et al. 2017, *NatCo*, **8**, 14906
- Tagawa, H., Haiman, Z., Bartos, I., & Kocsis, B. 2020a, *ApJ*, **899**, 26
- Tagawa, H., Haiman, Z., & Kocsis, B. 2020b, *ApJ*, **898**, 25
- Tagawa, H., Kocsis, B., Haiman, Z., et al. 2021, *ApJ*, **908**, 194
- Talbot, C., & Thrane, E. 2017, *PhRvD*, **96**, 023012
- Talbot, C., & Thrane, E. 2018, *ApJ*, **856**, 173
- Tanikawa, A., Kinugawa, T., Yoshida, T., Hijikawa, K., & Umeda, H. 2020, arXiv:2010.07616
- Thrane, E., & Talbot, C. 2019, *PASA*, **36**, e010
- Tiwari, V., & Fairhurst, S. 2020, arXiv:2011.04502
- Van Den Broeck, C. 2012, in Proc. 12th Marcel Grossmann Meeting on General Relativity, ed. A. H. Chamseddine (Singapore: World Scientific Publishing Co. Pte. Ltd.), 1682
- Van Den Broeck, C. 2014, *JPhCS*, **484**, 012008
- Vangioni, E., Olive, K., Prestegard, T., et al. 2015, *MNRAS*, **447**, 2575
- Venumadhav, T., Zackay, B., Roulet, J., Dai, L., & Zaldarriaga, M. 2020, *PhRvD*, **101**, 083030
- Vitale, S. 2016, *PhRvD*, **94**, 121501
- Vitale, S. 2020, arXiv:2007.05579
- Vitale, S., & Evans, M. 2017, *PhRvD*, **95**, 064052
- Vitale, S., Farr, W. M., Ng, K., & Rodriguez, C. L. 2019, *ApJL*, **886**, L1
- Vitale, S., Lynch, R., Sturani, R., & Graff, P. 2017, *CQGra*, **34**, 03LT01
- Vitale, S., & Whittle, C. 2018, *PhRvD*, **98**, 024029
- Wong, K., Franciolini, G., De Luca, V., et al. 2021a, *PhRvD*, **103**, 023026
- Wong, K. W., Breivik, K., Kremer, K., & Callister, T. 2021b, *PhRvD*, **103**, 083021
- Wysocki, D., Lange, J., & O’Shaughnessy, R. 2019, *PhRvD*, **100**, 043012
- Yang, Y., Bartos, I., Haiman, Z., et al. 2020, *ApJ*, **896**, 138
- Yang, Y., Bartos, I., Gayathri, V., et al. 2019, *PhRvL*, **123**, 181101
- Yi, S.-X., & Cheng, K. 2019, *ApJL*, **884**, L12
- Yu, H., Martynov, D., Vitale, S., et al. 2018, *PhRvL*, **120**, 141102
- Zevin, M., Bavera, S. S., Berry, C. P., et al. 2021, *ApJ*, **910**, 152
- Zevin, M., Pankow, C., Rodriguez, C. L., et al. 2017, *ApJ*, **846**, 82